Microfluid Nanofluid (2017) 21:14
DOI 10.1007/s10404-016-1839-6

RESEARCH PAPER

Inertially focused diamagnetic particle separation in ferrofluids

Yilong Zhou[1] · Le Song[2] · Liandong Yu[2] · Xiangchun Xuan[1]

Received: 10 November 2016 / Accepted: 16 December 2016

Abstract Continuous flow separation of target particles from a mixture is essential to many chemical and biomedical applications. There has recently been an increasing interest in the integration of active and passive particle separation techniques for enhanced sensitivity and flexibility. We demonstrate herein the proof-of-concept of a ferrofluid-based hybrid microfluidic technique that combines passive inertial focusing with active magnetic deflection to separate diamagnetic particles by size. The two operations take place in series in a continuous flow through a straight rectangular microchannel with a nearby permanent magnet. We also develop a three-dimensional numerical model to simulate the transport of diamagnetic particles during their inertial focusing and magnetic separation processes in the entire microchannel. The predicted particle trajectories are found to be approximately consistent with the experimental observations at different ferrofluid flow rates and ferrofluid concentrations.

Electronic supplementary material The online version of this article (doi:10.1007/s10404-016-1839-6) contains supplementary material, which is available to authorized users.

This article is part of the topical collection "2016 International Conference of Microfluidics, Nanofluidics and Lab-on-a-Chip, Dalian, China" guest edited by Chun Yang, Carolyn Ren and Xiangchun Xuan.

✉ Liandong Yu
liandongyu@hfut.edu.cn

✉ Xiangchun Xuan
xcxuan@clemson.edu

[1] Department of Mechanical Engineering, Clemson University, Clemson, SC 29634-0921, USA

[2] School of Instrument Science and Opto-electronic Engineering, Hefei University of Technology, Hefei 230009, China

Keywords Particle focusing · Particle separation · Inertial lift · Negative magnetophoresis · Microfluidics

1 Introduction

Continuous flow separation of target particles (either synthetic or biological) from a mixture is essential to many chemical and biomedical applications (Lenshof and Laurell 2010; Sajeesh and Sen 2014; Shields et al. 2015). It has been demonstrated in microfluidic devices by the use of a variety of field-driven techniques, which can be either active or passive depending on the nature of the driving force (Pamme 2007; Karimi et al. 2013). Active particle separation techniques use an externally applied force field (Gossett et al. 2010; Watarai 2013), ranging from acoustic (Laurell et al. 2007; Lin et al. 2012) to electric (Pethig 2010; Li et al. 2014), magnetic (Pamme 2006; Suwa and Watarai 2011; Hejazian et al. 2015) and optical (Kayani et al. 2012; Lee et al. 2012) forces, to remotely manipulate the suspended particles in fluid flows. They are usually capable of separating particles at a high resolution and purity but at the cost of throughput. Passive particle separation techniques exploit the flow-induced intrinsic lift and/or drag forces to direct particles toward different equilibrium positions (Tsutsui and Ho 2009; Gao et al. 2013), which cover deterministic lateral displacement (DLD) (Huang et al. 2004), hydrodynamic filtration (Yamada and Seki 2005), pinched flow fractionation (PFF) (Yamada et al. 2004), hydrophoresis (Choi et al. 2009), inertial focusing (Di Carlo 2009; Martel and Toner 2014; Amini et al. 2014; Zhang et al. 2016a) and elasto-inertial separation (Yang et al. 2011; Lu et al. 2015; Liu et al. 2015b), etc. They have the potential to attain high throughput, but most of them require a complex channel structure and/or a sophisticated flow control to achieve the separation resolution.

Published online: 13 January 2017

There has recently been an increasing interest in the integration of active and passive particle separation techniques for enhanced sensitivity and flexibility (Yan et al. 2016). Among those diverse hybrid microfluidic systems (Yan et al. 2016), the combination of active magnetic separation with passive inertial and/or elastic focusing shows good potentials due to their respective unique features. Magnetic field-driven particle separation has the advantages of low cost and heating free (with cheap off-the-shelf magnets), etc., over the other active separation techniques (Gijs 2004; Nguyen 2012; Cao et al. 2014; Yang et al. 2016; Zhao et al. 2016a). It utilizes magnetic field gradient induced positive (for magnetic particles or magnetically tagged cells, Pamme and Manz 2004; Inglis et al. 2006; Hoshino et al. 2011; Kang et al. 2012; Zhou and Wang 2016a) or negative (for diamagnetic particles in magnetic media, Zhu et al. 2010; Vojtíšek et al. 2012; Zhu et al. 2012a; Zeng et al. 2013; Hejazian and Nguyen 2016; Zhou and Wang 2016b; Zhao et al. 2016b) magnetophoresis to separate particles based on the difference in size (Zhu et al. 2012b; Liang and Xuan 2012), magnetization (Liang et al. 2013; Zhu et al. 2014) and shape (Zhou and Xuan 2016). Inertial and/or elastic particle focusing makes use of the flow-induced inertial (in Newtonian fluids, Di Carlo et al. 2007; Oakey et al. 2010; Choi et al. 2011; Chung et al. 2013; Zhou et al. 2013; Martel and Toner 2013; Wang et al. 2015; Li et al. 2016) or elasto-inertial (in non-Newtonian fluids, Leshansky et al. 2007; Kim et al. 2012; Kang et al. 2013; Romeo et al. 2013; Lim et al. 2014; Cha et al. 2014; Yuan et al. 2015; Xiang et al. 2016a, b) lift forces to focus particles toward one or multiple equilibrium positions in simple microchannels at a medium to high throughput.

Along the direction of integrated microfluidic magnetic separation and inertial/elastic focusing systems, two groups (Kim et al. 2016; Zhang et al. 2016b) have recently demonstrated the use of a viscoelastic polymer-mixed ferrofluid for a continuous sheath-free diamagnetic particle separation. The polymer flow-induced elasto-inertial lift focuses particles to the channel centerline and the ferrofluid-induced magnetic force deflects the pre-aligned particles toward size-dependent flow paths. A similar idea has also been reported in an earlier paper (Del Giudice et al. 2015) to separate magnetic particles from diamagnetic particles in a polymer solution, where the elasto-inertial prefocusing effect significantly reduces the number of magnetic particles that either escape from the collection or get stuck onto the near-magnet wall. In another study (Ozkumur et al. 2013), inertial focusing has been used to position a mixture of white blood cells and magnetically labeled circulating tumor cells (which was extracted from blood using a separate DLD device) in a serpentine microchannel prior to separating them by magnetization using a quadrupole magnetic circuit.

In this work, we develop based upon the earlier studies (Ozkumur et al. 2013; Del Giudice et al. 2015; Kim et al. 2016; Zhang et al. 2016a, b) a ferrofluid-based microfluidic device for inertially focused label-free separation of diamagnetic particles. The two operations are integrated into a straight rectangular microchannel with a nearby permanent magnet for easy fabrication and flow control. We also develop a three-dimensional numerical model to simulate the diamagnetic particle transport in ferrofluid flow through the entire microchannel. The effects of ferrofluid flow rate and concentration on the inertial particle focusing and diamagnetic particle separation are investigated both experimentally and numerically.

2 Experiment

2.1 Microfluidic chip fabrication

Figure 1 shows a picture of the microfluidic chip used in our experiments, which was fabricated with polydimethylsiloxane (PDMS) using a custom-modified soft lithography method as detailed elsewhere (Zhu et al. 2012a). The straight rectangular microchannel is 2 cm long and 65 μm wide, followed by a 2 mm long, 960 μm wide expansion for enhanced particle separation and visualization. The channel is uniformly 35 μm high and hence has an aspect ratio (=width/height) of 1.86. Two stacked neodymium-iron-boron permanent magnets (B221, 1/8″ × 1/8″ × 1/16″, K&J Magnets, Inc.) were embedded into the PDMS slab. They were placed in direct contact with the glass slide and positioned 700 μm (edge to edge distance) away from the outlet expansion, which was performed under a microscope using the approach described in Zhu et al. 2012a). Their magnetization direction is through the 1/16″ thickness and perpendicular to the flow direction. As seen from the top-view channel picture in Fig. 1, the magnets had to be placed below the lower corner of the channel expansion due to a limited working space. This configuration, as explained later, can cause a significant buildup of ferrofluid nanoparticles near the corner, which should be avoided in future designs.

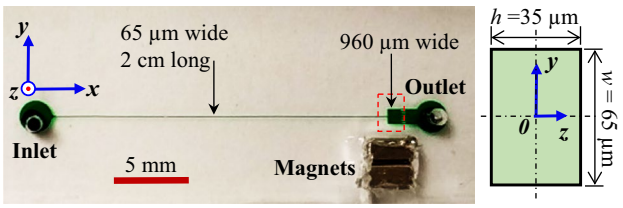

Fig. 1 Picture of the microfluidic chip with the relevant channel dimensions and coordinates being labeled in the *top* (*left*) and cross-sectional (*right*) views. Two stacked permanent magnets are embedded into the PDMS slab and placed nearby the outlet expansion. The *dashed-line box* highlights the window of view for particle visualization at the outlet expansion

2.2 Particle solution preparation and experimental method

Spherical diamagnetic polystyrene particles with 10 μm (plain, Sigma Aldrich) and 20 μm (fluorescent, Phosphorex, Inc.) in diameter were mixed and re-suspended into EMG 408 ferrofluid (Ferrotec Corp.) whose concentration was varied by dilution with water. The mass density of each type of particles is 1.05 g/cm^3, and that of the ferrofluid as received (without any dilution) is 1.07 g/cm^3. 0.5% (in volume) Tween 20 (Fisher Scientific) was added to the suspension to reduce particle aggregations and adhesions to channel walls. Particulate solution was driven through the microchannel by an infusion syringe pump (KD Scientific) and drained out via a PFA tubing (IDEX Health & Science) connected to the channel outlet. Particle motions at the outlet expansion (see the window of view in Fig. 1) were visualized and recorded through an inverted fluorescent microscope (Nikon Eclipse TE2000U, Nikon Instruments) with a CCD camera (Nikon DS-Qi1Mc) at a rate of approximately 12 frames per second. Fluorescent and bright-field lights were used concurrently to visualize both fluorescent (appearing bright) and plain (appearing dark) particles. Captured digital videos and images were post-processed using the Nikon imaging software (NIS-Elements AR 2.30). Superimposed images of fluorescent and plain particles were each obtained by stacking the same sequence of snapshot images with the maximum and minimum intensity projections, respectively, from videos with a minimum duration of 30 s (i.e., over 300 consecutive frames).

3 Simulation

We use the schematic in Fig. 2 to briefly explain the working mechanism of the proposed ferrofluid-based microfluidic particle separator in Fig. 1. The flow-induced inertial lift, $\mathbf{F}_\mathrm{L}$, focuses particles toward the center-plane of a straight rectangular microchannel with a large aspect ratio (=width/height) (Zhou and Papautsky 2013; Lu and Xuan 2015; Liu et al. 2015a). The magnetic force, $\mathbf{F}_\mathrm{M}$, generated in the ferrofluid deflects the inertially focused diamagnetic particles away from the magnet at a size-dependent rate, yielding a continuous label-free separation at the expansion of the microchannel. To understand and predict this inertially focused diamagnetic particle separation, we developed a 3D numerical model to simulate particle motions in ferrofluid flow through the entire microchannel. Our model was based on the Lagrangian tracking method, which considered only the one-way actions that the flow (via the drag and lift forces) and magnetic (via the magnetic force) fields have on the suspended particles. Considering the small Stokes number in our experiments, we assumed

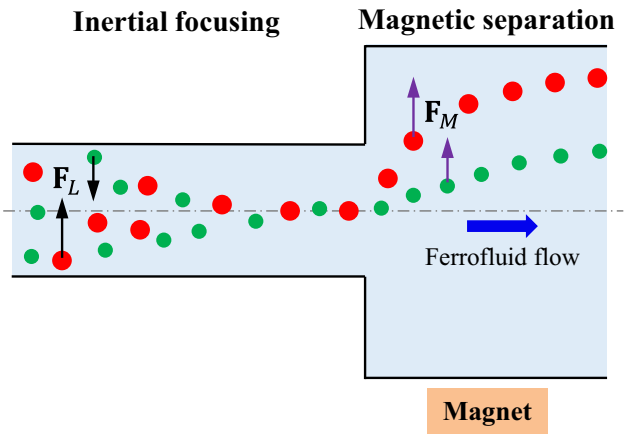

Fig. 2 Schematic diagram (not drawn to scale) illustrating the mechanism of particle focusing and separation for the proposed ferrofluid-based microfluidic device in Fig. 1. The flow-induced inertial lift, $\mathbf{F}_\mathrm{L}$, prefocuses a mixture of diamagnetic particles that are then displaced by the ferrofluid-enabled magnetic force, $\mathbf{F}_\mathrm{M}$, toward size-dependent flow paths

particles follow the fluid flow in the streamwise direction and instantly attain their terminal velocities in the cross-stream direction, i.e.,

$$\mathbf{u}_\mathrm{p} = \mathbf{u} + \frac{\mathbf{F}_\mathrm{L} + \mathbf{F}_\mathrm{M}}{3\pi\eta a K} \tag{1}$$

where $\mathbf{u}_\mathrm{p}$ is the particle velocity, $\mathbf{u}$ is the ferrofluid velocity, η is the ferrofluid viscosity, a is the particle diameter, and K is the correction factor for Stokes' drag due to the wall effects. Note that we have assumed Stokes' drag in Eq. (1) because the Reynolds number based on the transverse particle migration velocity is small (Di Carlo et al. 2007). The gravity effect on particle motion was neglected considering the nearly equal density of polystyrene particles to that of the suspending ferrofluid. The following subsections explain how we treated the terms in Eq. (1) and how we simulated the particle trajectories.

3.1 Inertial lift, $\mathbf{F}_\mathrm{L}$

Following the literature (Ho and Leal 1974; Asmolov 1999), we use the following form of formula to compute the two components of the inertial lift, $F_{\mathrm{L\_y}}$ and $F_{\mathrm{L\_z}}$, in the channel width (y) and height (z) directions (see Fig. 1),

$$F_{\mathrm{L\_y}} = C_{\mathrm{L\_y}}\rho U_\mathrm{m}^2 a^2 \kappa^2 \quad \text{and} \quad F_{\mathrm{L\_z}} = C_{\mathrm{L\_z}}\rho U_\mathrm{m}^2 a^2 \kappa^2 \tag{2}$$

where $C_{\mathrm{L\_y}}$ and $C_{\mathrm{L\_z}}$ are the dimensionless lift coefficient in the y and z directions (see Fig. 1), respectively, ρ is the fluid density, U_m is the maximum fluid velocity in the channel length (x) direction, and $\kappa = a/h$ is the particle blockage ratio with h being the channel height (which is the smaller dimension of the channel cross section). We note

that each lift coefficient is a function of Reynolds number, $Re = \rho U_m h/\eta$, channel aspect ratio, AR $= w/h$ with w being the channel width, particle blockage ratio, κ, and particle lateral position, (y, z) (Liu et al. 2015a, 2016). We obtained the following approximate formulae for the two lift coefficients by curve fitting the direct numerical simulation data in Liu et al. (2016) (see Figs. S-1 and S-2 in the Supplementary Material),

$$C_{L\_y} = \frac{(-0.006Re + 2.2)(-0.1\kappa + 1.34)}{2.096} \times \begin{pmatrix} -0.1903y^{*6} + 0.6015y^{*5} - 0.6534y^{*4} \\ +0.2687y^{*3} - 0.0253y^{*2} + 0.0361y^{*} \end{pmatrix} \quad (3)$$

$$C_{L\_z} = \frac{(-0.006Re + 2.2)(-0.1\kappa + 1.34)}{2.8427} \times \left(-3.2427z^{*3} + 0.0059z^{*2} + 0.7409z^{*}\right) \quad (4)$$

where the pre-factor in each equation was used to account for the influence of Reynolds number and particle blockage ratio on lift coefficient (Liu et al. 2016), $y^* = 2y/h$ and $z^* = 2z/h$ are the normalized particle positions in the channel width (y) and height (z) directions, respectively.

3.2 Magnetic force, $\mathbf{F}_M$

The magnetic force experienced by a diamagnetic particle in a ferrofluid, $\mathbf{F}_M$, can be expressed as (Rosensweig 1987),

$$\mathbf{F}_M = -\frac{1}{6}\pi a^3 \mu_0 (\mathbf{M}_f \cdot \nabla)\mathbf{H} \quad (5)$$

where μ_0 is the permeability of the free space, $\mathbf{H}$ is the magnetic field vector at the particle center. The ferrofluid magnetization, $\mathbf{M}_f$, is given by (Rosensweig 1987),

$$\mathbf{M}_f = c_0 \mathbf{M}_d [\coth(\alpha) - 1/\alpha] \quad (6)$$

$$\alpha = \frac{\pi d^3 \mu_0 M_d H}{6 k_B T} \quad (7)$$

where c_0 is the volume fraction of ferrofluid (superparamagnetic) nanoparticles, $\mathbf{M}_d$ is the saturation moment of ferrofluid nanoparticles of diameter d with M_d being the magnitude, k_B is the Boltzmann constant, and T is the ferrofluid temperature. Note that the contribution from the diamagnetic particle magnetization has been neglected in Eq. (5) because the magnetic susceptibility of polystyrene particles (on the order of 10^{-6}) (Tarn et al. 2009; Shen et al. 2012) is at least 4 orders of magnitude smaller than that of the ferrofluid used in our experiments (on the order of 0.1, Ferrotec Corp.).

3.3 Correction factor, K, for Stokes' drag

As the size of the particles used in our experiments is comparable to the channel height, we considered the retardation effects from both the top and bottom channel walls on transverse particle migrations that are parallel and normal to them via $K_{\parallel}$ and $K_{\perp}$, respectively (Happel and Brenner 1973). We assumed each correction factor is simply a product of those from the top and bottom channel walls, i.e.,

$$K_{\parallel} = K_{\parallel\_top} \times K_{\parallel\_bot} = f\left(\frac{a/2}{\delta}\right) \times f\left(\frac{a/2}{h-\delta}\right) \quad (8)$$

$$f(x) = \left(1 - \frac{9}{16}x + \frac{1}{8}x^3 - \frac{45}{256}x^4 - \frac{1}{16}x^5\right)^{-1} \quad (9)$$

$$K_{\perp} = K_{\perp\_top} \times K_{\perp\_bot} = g\left(\frac{a/2}{\delta}\right) \times g\left(\frac{a/2}{h-\delta}\right) \quad (10)$$

$$g(x) = \left(1 - \frac{9}{8}x + \frac{1}{2}x^3\right)^{-1} \quad (11)$$

where δ is the perpendicular distance from the particle center to either the top or bottom channel wall, $f(x)$ and $g(x)$ are the functions of the correction factors for particle motions parallel and normal to a single channel wall (Happel and Brenner 1973), respectively. Note that the two values for x, i.e., $(a/2)/\delta$ or $(a/2)/(h-\delta)$, represent the relative particle–wall distances for the two walls.

3.4 Numerical method

We developed a 3D numerical model in COMSOL® 5.2 to solve the Navier–Stokes equations for the ferrofluid velocity field in the entire microchannel. The ferrofluid concentration was assumed uniform in order to avoid considering the full coupling between the ferrofluid flow and concentration fields that has been demonstrated to significantly complicate the model (Zhou et al. 2015). The magnetic field was obtained using the analytical formulae from Furlani (2001) for rectangular permanent magnets that were input to COMSOL as variables. Particle motions were traced using the intrinsic Streamline function in COMSOL via the particle velocity in Eq. (1). Particles' initial positions at the channel inlet were set to be at least one half-diameter away from any channel walls to account for the steric effects. Other settings of the model and material properties involved in the simulation can be referred to our earlier papers (Zhou et al. 2015, 2016).

4 Results and discussion

4.1 Inertial particle focusing at different ferrofluid flow rates

Figure 3 demonstrates the inertial focusing of a mixture of 20 μm (top row, fluorescent) and 10 μm (middle row, plain) polystyrene particles in 0.5 × EMG 408 ferrofluid in the absence of magnets. Consistent with previous studies (Zhou and Papautsky 2013; Lu and Xuan 2015; Liu et al. 2015a), the flow-induced inertial lift directs both types of particles toward the center of the longer side in a high aspect ratio (AR = 1.86) rectangular channel, i.e., the channel centerline on the top-view images in Fig. 3. Moreover, as expected from Eq. (2), this inertial particle focusing increases with the ferrofluid flow rate and is a strong function of particle size. The superimposed images in Fig. 3 indicate that 20 μm particles (top row) receive a fairly good focusing at a flow rate greater than 0.5 ml/h. In contrast, 10 μm particles (middle row) need a flow rate of above 1 ml/h to achieve a similar inertial focusing, which appears to be consistent with our recent work (Lu and Xuan 2015). These dependences of inertial focusing on flow rate and particle size are both reasonably predicted by our numerical simulations in the bottom row of Fig. 3 (green and red lines for 10 and 20 μm particles, respectively).

4.2 Diamagnetic particle separation at different ferrofluid flow rates

Figure 4 shows the magnetic deflection and separation of a mixture of inertially focused 10 μm (left column, plain) and 20 μm (middle column, fluorescent) polystyrene particles in 0.5 × EMG 408 ferrofluid at the outlet expansion. Both types of particles are pushed away from the magnets (which are located below the lower sidewall, see Fig. 1) by negative magnetophoresis. At the flow rate of 0.5 ml/h, 20 μm particles can all reach the upper sidewall of the outlet expansion due to their strong magnetophoretic motions. In contrast, 10 μm particles cover nearly the top-half of the expansion due to both the weaker inertial focusing and the weaker magnetic deflection than 20 μm particles. At the flow rate of 0.8 ml/h, 20 μm particles can no longer reach the upper sidewall due to their reduced residence time in experiencing magnetophoresis. Their magnetic deflection is, however, greater than that of the inertially focused

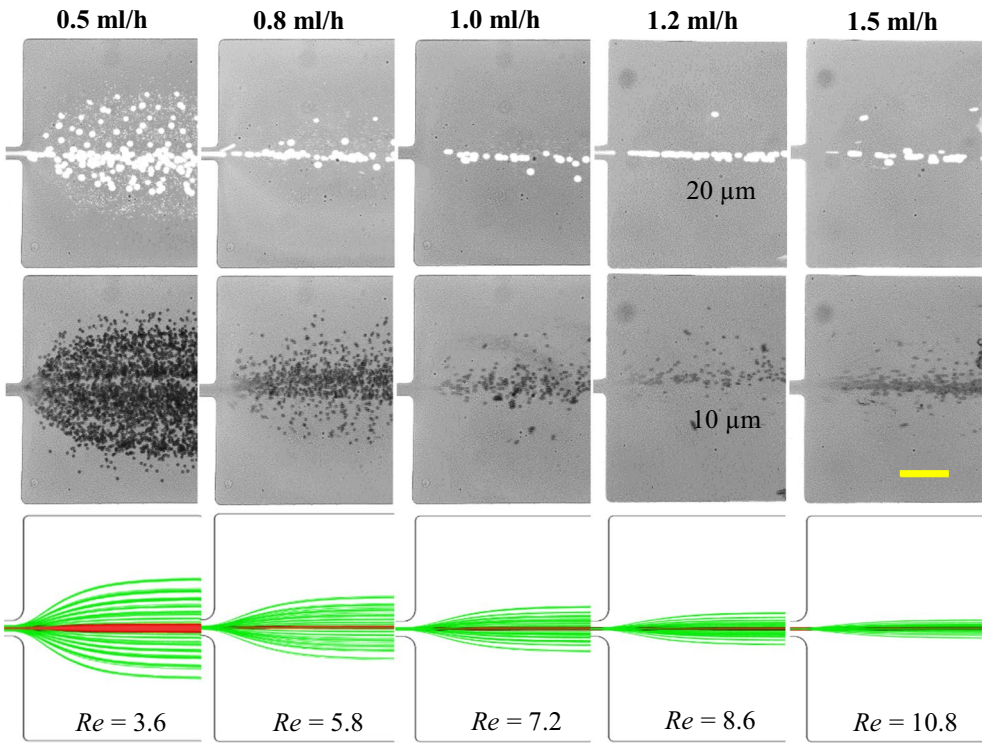

Fig. 3 Inertial focusing of a particle mixture in 0.5 × EMG 408 ferrofluid at the outlet expansion under different flow rates in the absence of magnetic field: superimposed images of 20 μm fluorescent particles (*top row*) and 10 μm plain particles (*middle row*), and numerically predicted particle trajectories (*bottom row*, *red lines* for 20 μm particles and *green lines* for 10 μm particles). The calculated values of *Re* are labeled on the *bottom row*. The flow direction is from to *left* to *right* in all images. The *scale bar* represents 200 μm (color figure online)

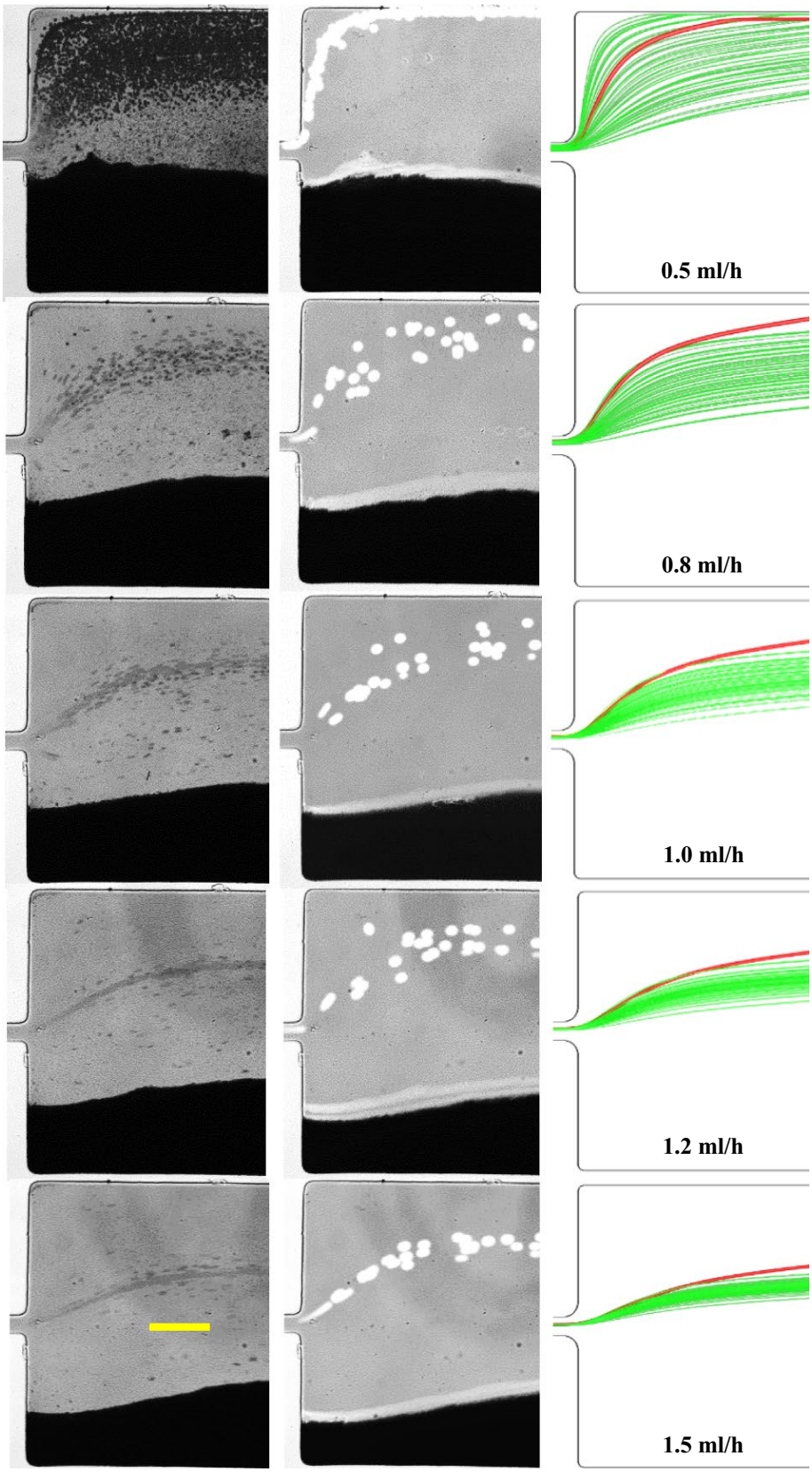

Fig. 4 Magnetic separation of a mixture of inertially focused diamagnetic particles in 0.5 × EMG 408 ferrofluid at the outlet expansion under different flow rates: superimposed images of 10 μm plain particles (*left column*) and 20 μm fluorescent particles (*middle column*), and numerically predicted particle trajectories (*green lines* for 10 μm particles and *red lines* for 20 μm particles). The black zones at the *lower corner* of the expansion are the buildup of ferrofluid nanoparticles due to positive magnetophoresis in a locally weak fluid flow. The flow direction is from to *left* to *right* in all images. The *scale bar* represents 200 μm (color figure online)

10 μm particles, leading to a size-based particle separation at the outlet expansion. The separation distance grows at the flow rate of 1 ml/h due to primarily the enhanced inertial focusing and hence a lowered dispersion of 10 μm particles. Further increasing the flow rate does not significantly improve the particle separation due to the reduced displacement of both types of particles.

We note in Fig. 4 that the magnetically deflected 20 μm particles exhibit a relative large dispersion as compared to their fairly good inertial focusing in Fig. 3. In fact, the dispersion of 20 μm particles is visually even greater than that of 10 μm particles in Fig. 4 except for the lowest flow rate. We attribute this unexpected phenomenon to the relative large size deviation (at least ±3 μm as measured with a microscope) of 20 μm particles, which, though not strongly affecting the inertial focusing performance because our microchannel is sufficiently long, can cause considerable variations in magnetophoretic migration at the outlet expansion. We also note there is a significant buildup of ferrofluid nanoparticles at the lower corner of the outlet expansion in Fig. 4. This is, as expected, due to positive magnetophoresis of the superparamagnetic nanoparticles in a locally weak fluid flow (Tsai et al. 2007) under a strong non-uniform magnetic field (note the magnets were placed right below the lower corner of the expansion, see Fig. 1). With the increase in ferrofluid flow rate, the nanoparticle buildup is mitigated due to the increasing shear stress. The accumulated nanoparticles are expected to affect the ferrofluid properties (e.g., concentration and viscosity) and hence the diamagnetic particle deflection. This issue can be minimized by the use of a longer outlet expansion such that the magnets can be placed further downstream. Alternatively, the magnets can be placed upstream with a distance away from the expansion, where the microchannel will have to be long enough for inertial particle focusing.

In addition, we admit that the ferrofluid becomes non-uniform even inside the microchannel due to the strong action of permanent magnets on nanoparticles (Zhou et al. 2016). We did not consider the resultant non-uniform ferrofluid properties in our model for simplicity, which turns out to still correctly predict the decreasing trend of diamagnetic particle deflection with increasing ferrofluid flow rate in Fig. 4 (right column). However, the extent of particle deflection in the simulation seems to be overall smaller than that in the experiment, which can be better viewed from the direct comparison between the experimentally measured and numerically predicted particle positions in Fig. 5. The experimental data were obtained from the images in Fig. 4, which were measured at the position of the highest particle concentration with respect to the channel centerline at the outlet expansion. Error bars were included to cover the span of particle streams. The

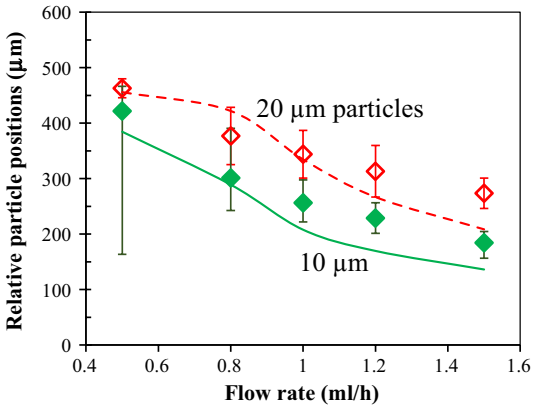

Fig. 5 Comparison of the experimentally measured (*symbols* with *error bars*) and numerically predicted (*lines*) particle positions at the outlet expansion for inertially focused 10 and 20 μm diamagnetic particle separation in 0.5 × EMG 408 ferrofluid at different flow rates. The experimental and numerical data were measured directly from the corresponding images in Fig. 4 with respect to the channel centerline. Note that the *error bar* for each data point covers the measurements from at least 25 particles of 20 μm diameter or at least 100 particles of 10 μm diameter

numerical data were measured at the center of the predicted particle trajectories in Fig. 4. For clarity, the predicted dispersion of 10 μm particles due to insufficient inertial focusing was not included in Fig. 5. As the discrepancy between the experimental and numerical results in Fig. 5 gets larger at higher flow rates, it does not seem to be strongly correlated with the decreasing buildup of ferrofluid nanoparticles in Fig. 4. A complete separation of 10 and 20 μm particles (i.e., no overlap between the two particle streams with 100% separation efficiency and purity) is achieved experimentally for flow rate ranging from 1 to 1.5 ml/h (see Fig. 5). In contrast, the numerically predicted complete separation occurs in the range of 0.5 to 1 ml/h (see the right column of Fig. 4). This discrepancy may be due to the ferrofluid buildup that has been neglected in the numerical model.

We also studied the separation of a mixture of 10 and 15 μm diamagnetic particles in the same fluid-channel system under identical experimental conditions (see Fig. S-3 in Supplementary Material for the experimental images and numerical predictions). A good separation was observed to take place at the flow rate of around 1 ml/h, which is consistent with that of 10 and 20 μm particles. However, the discrepancy between experimental and simulation results still exists in this separation (see Fig. S-4 in the Supplementary Material), which may be due to the neglect of the influences from particles (which are comparable to the channel dimensions) onto the flow and magnetic fields. Further studies are needed on this aspect.

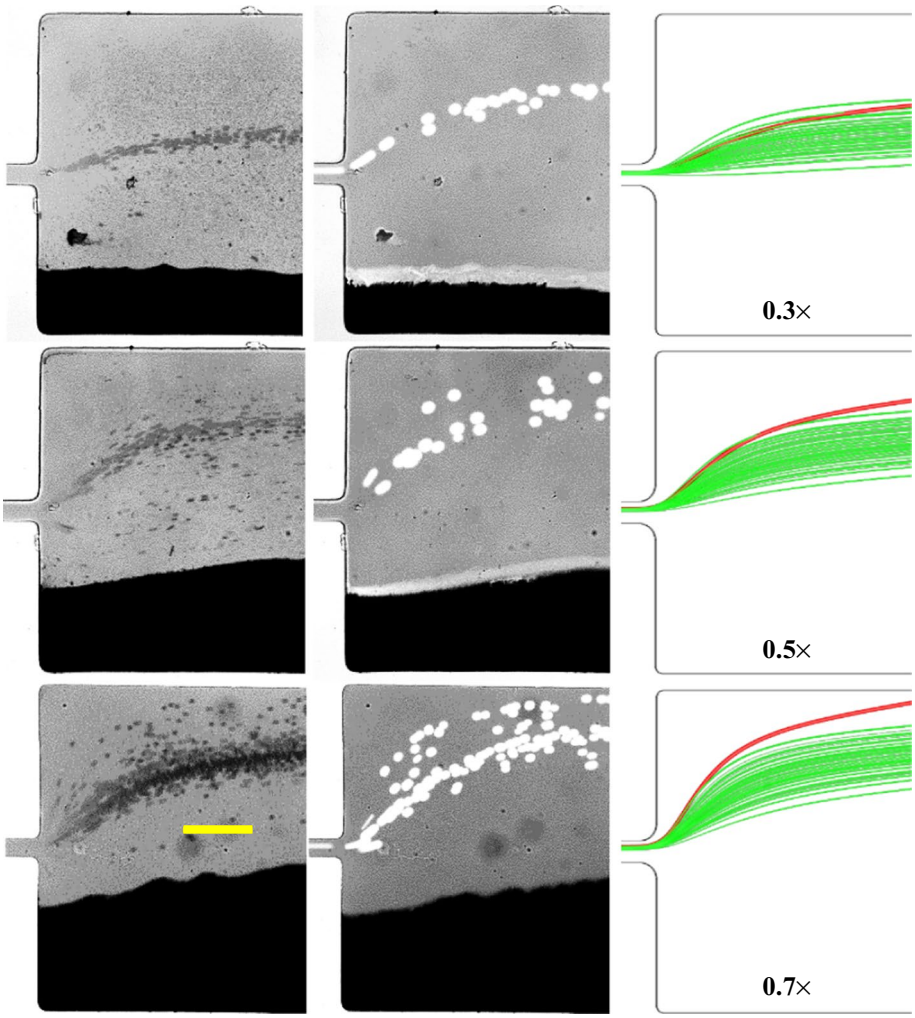

Fig. 6 Inertially focused diamagnetic particle separation in EMG 408 ferrofluid of different concentrations at a constant flow rate of 1 ml/h: superimposed images of 10 μm plain particles (*left column*) and 20 μm fluorescent particles (*middle column*), and numerically predicted particle trajectories (*green lines* for 10 μm particles and *red lines* for 20 μm particles). The black zones at the *lower corner* of the expansion are the buildup of ferrofluid nanoparticles via positive magnetophoresis. The flow direction is from to *left* to *right* in all images. The *scale bar* represents 200 μm (color figure online)

4.3 Diamagnetic particle separation in ferrofluids of different concentrations

Figure 6 shows the effect of ferrofluid concentration on the magnetic separation of a mixture of inertially focused 10 and 20 μm polystyrene particles at a fixed flow rate of 1 ml/h. As the ferrofluid density and viscosity do not change significantly with its concentration, the flow-induced inertial lift force remains nearly unvaried. Therefore, the two types of particles should each achieve a similar extent of inertial focusing in the range from 0.3 × to 0.7 × EMG 408 ferrofluid. However, as the magnetic force is a linear function of ferrofluid concentration, the magnetic deflection of each type of particles increases at a higher ferrofluid concentration as viewed from the superimposed images in Fig. 6 (left and middle columns for 10 and 20 μm particles, respectively). This should in theory yield a greater separation distance with the increasing ferrofluid concentration unless 20 μm particles are deflected all the way to the upper sidewall. Such an analysis is indeed supported by our simulation results in Fig. 6 (right column), which was, however, not observed in our experiment. We attribute this inconsistency to mainly the large dispersion of 20 μm particles, which, as noted earlier, may result from their relative size deviations. Another potential factor is the growing ferrofluid nanoparticle buildup at the lower corner of the outlet expansion with the increasing ferrofluid concentration, which, as viewed from the experimental images in Fig. 6, may be responsible for the increased dispersion of 10 μm particles.

Figure 7 shows a quantitative comparison of the particle positions measured at the outlet expansion from the experimental and numerical images in Fig. 6. An approximately linear curve is predicted for the magnetic deflections of both 10 and 20 μm particles versus ferrofluid concentration. This relationship comes from the theoretically linear dependence of magnetophoretic particle motion on ferrofluid concentration. In contrast, the experimentally observed magnetic deflection of each type of particles exhibits a flattened out increase at higher ferrofluid concentrations. This trend may be associated with the increasing buildup of ferrofluid nanoparticles at the outlet expansion

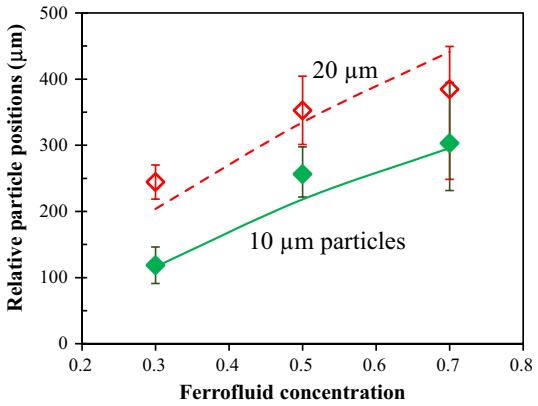

Fig. 7 Comparison of the experimentally measured (*symbols* with *error bars*) and numerically predicted (*lines*) particle positions at the outlet expansion for inertially focused 10 and 20 μm diamagnetic particle separation in EMG 408 ferrofluid of different concentrations. The ferrofluid flow rate was fixed at 1 ml/h. The experimental and numerical data were measured directly from the images in Fig. 6 with respect to the channel centerline

as viewed from the experimental images in Fig. 6. Further studies are required in order to elucidate this mechanism, where the magnets need to be placed distant away from the corner of the outlet expansion.

5 Conclusions

We have demonstrated the proof-of-concept of a hybrid microfluidic technique for sheathless label-free diamagnetic particle separation in ferrofluid flows through a straight rectangular microchannel. This separation technique utilizes the flow-induced inertial lift to focus a mixture of particles into a narrow stream along the channel centerline, and the ferrofluid-induced magnetic force to deflect the pre-aligned diamagnetic particles toward size-dependent flow paths. It has the potential to separate particles by multiple parameters including size, shape (Zhou and Xuan 2016), and magnetization (Liang et al. 2013; Ozkumur et al. 2013; Zhu et al. 2014). We have also developed a 3D numerical model to predict and understand the diamagnetic particle transport during the sequential focusing and separation processes under various experimental conditions. The numerical predictions are found to be approximately consistent with the experimental observations. We note that our current device has a design defect, which can draw a significant buildup of ferrofluid nanoparticles at the corner of the channel expansion. The resulting changes in ferrofluid properties and flow pattern are neglected in our model, which may be responsible, at least partially, for the discrepancy between the experimental and numerical results. Further studies will be performed on this aspect.

Acknowledgements This work is supported by NSF under grant CBET-1150670 (X. Xuan). The support from University 111 Project of China under Grant B12019 is also gratefully acknowledged (L. Yu). In addition, the authors thank Dr. Chao Liu and Prof. Guoqing Hu for providing the direct numerical simulation data in their Lab Chip paper (2016) that were used to obtain the curve-fitted formulae for inertial lift coefficients.

References

Amini H, Lee W, Di Carlo D (2014) Inertial microfluidic physics. Lab Chip 14:2739–2761

Asmolov ES (1999) The inertial lift on a spherical particle in a plane Poiseuille flow at large channel Reynolds number. J Fluid Mech 381:63–87

Cao Q, Han X, Li L (2014) Configurations and control of magnetic fields for manipulating magnetic particles in microfluidic applications: magnet systems and manipulation mechanisms. Lab Chip 14:2762–2777

Cha S, Kang K, You JB, Im SG, Kim Y, Kim JM (2014) Hoop stress-assisted three-dimensional particle focusing under viscoelastic flow. Rehol Acta 53:927–933

Choi S, Song S, Choi C, Park JK (2009) Microfluidic self-sorting of mammalian cells to achieve cell cycle synchrony by hydrophoresis. Anal Chem 81:1964–1968

Choi YS, Seo KW, Lee SJ (2011) Lateral and cross-lateral focusing of spherical particles in a square microchannel. Lab Chip 11:460–465

Chung AJ, Pulido D, Oka JC, Amini H, Masaeli M, Di Carlo D (2013) Microstructure-induced helical vortices allow single-stream and long-term inertial focusing. Lab Chip 13:2942–2949

Del Giudice F, Madadi H, Villone MM, D'Avino G, Cusano AM, Vecchione R, Ventre M, Maffettone PL, Netti PA (2015) Magnetophoresis 'meets' viscoelasticity: deterministic separation of magnetic particles in a modular microfluidic device. Lab Chip 15:1912–1922

Di Carlo D (2009) Inertial microfluidics. Lab Chip 9:3038–3046

Di Carlo D, Irimia D, Tompkins RG, Toner M (2007) Continuous inertial focusing, ordering, and separation of particles in microchannels. Proc Natl Acad Sci 104:18892–18897

Furlani EP (2001) Permanent magnet and electromechanical devices: materials, analysis, and applications. Academic Press, Cambridge

Gao Y, Li W, Pappas D (2013) Recent advances in microfluidic cell separations. Analyst 138:4714–4721

Gijs MAM (2004) Magnetic bead handling on-chip: new opportunities for analytical applications. Microfluid Nanofluid 1:22–40

Gossett DR, Weaver WM, Mach AJ, Hur SC, Tse HT, Lee W, Amini H, Di Carlo D (2010) Label-free cell separation and sorting in microfluidic systems. Anal Bioanal Chem 397:3249–3267

Happel J, Brenner H (1973) Low Reynolds number hydrodynamics. Prentice-Hall, Englewood Cliffs

Hejazian M, Nguyen NT (2016) Magnetofluidic concentration and separation of non-magnetic particles using two magnet arrays. Biomicrofluid 10:044103

Hejazian M, Li W, Nguyen NT (2015) Lab on a chip for continuous-flow magnetic cell separation. Lab Chip 15:959–970

Ho BP, Leal LG (1974) Inertial migration of rigid spheres in two-dimensional unidirectional flows. J Fluid Mech 65(02):365–400

Hoshino K, Huang YY, Lane N, Huebschman M, Uhr JW, Frenkel EP, Zhang X (2011) Microchip-based immunomagnetic detection of circulating tumor cells. Lab Chip 11:3449–3457

Huang L, Cox EC, Austin RH, Sturm JC (2004) Continuous particle separation through deterministic lateral displacement. Science 304:987–990

Inglis DW, Riehn R, Sturm JC, Austin RH (2006) Microfluidic high gradient magnetic cell separation. J Appl Phys 99:08K101

Kang JH, Krause S, Tobin H, Mammoto A, Kanapathipillai M, Ingber DE (2012) A combined micromagnetic-microfluidic device for rapid capture and culture of rare circulating tumor cells. Lab Chip 12:2175–2181

Kang K, Lee SS, Hyun K, Lee SJ, Kim JM (2013) DNA-based highly tunable particle focuser. Nat Commun 4:2567. doi:10.1038/ncomms3567

Karimi A, Yazdi S, Ardekani AM (2013) Hydrodynamic mechanisms of cell and particle trapping in microfluidics. Biomicrofluid 7:021501

Kayani AA, Khoshmanesh K, Ward SA, Mitchell A, Kalantar-Zadeh K (2012) Optofluidics incorporating actively controlled micro- and nano-particles. Biomicrofluid 6:031501

Kim JY, Ahn SW, Lee SS, Kim JM (2012) Lateral migration and focusing of colloidal particles and DNA molecules under viscoelastic flow. Lab Chip 12:2807–2814

Kim MJ, Lee DJ, Youn JR, Song YS (2016) Two step label free particle separation in a microfluidic system using elasto-inertial focusing and magnetophoresis. RSC Adv 6:32090–32097

Laurell T, Petersson F, Nilsson A (2007) Chip integrated strategies for acoustic separation and manipulation of cells and particles. Chem Soc Rev 36:492–506

Lee KS, Yoon SY, Kim SB, Lee KH, Sung HJ, Kim SS (2012) Assessment of cross-type optical particle separation system. Microfluid Nanofluid 13:9–17

Lenshof A, Laurell T (2010) Continuous separation of cells and particles in microfluidic systems. Chem Soc Rev 39:1203–1217

Leshansky AM, Bransky A, Korin N, Dinnar U (2007) Tunable nonlinear viscoelastic "focusing" in a microfluidic device. Phys Rev Lett 98:234501

Li M, Li WH, Zhang J, Alici G, Wen W (2014) A review of microfabrication techniques and dielectrophoretic microdevices for particle manipulation and separation. J Phys D 47(6):063001

Li M, Munoz HE, Schmidt A, Guo B, Lei C, Goda K, Di Carlo D (2016) Inertial focusing of ellipsoidal *Euglena gracilis* cells in a stepped microchannel. Lab Chip 16:4458–4485

Liang L, Xuan X (2012) Continuous sheath-free magnetic separation of particles in a U-shaped microchannel. Biomicrofluid 6:044106

Liang L, Zhang C, Xuan X (2013) Enhanced separation of magnetic and diamagnetic particles in a dilute ferrofluid. Appl Phys Lett 102:234101

Lim EJ, Ober T, Edd JF, Desai SP, Neal D, Bong KW, Doyle PS, McKinley GH, Toner M (2014) Inertio-elastic focusing of bioparticles in microchannels at high throughput. Nat Commun 5:4120. doi:10.1038/ncomms5120

Lin SC, Mao X, Huang TJ (2012) Surface acoustic wave (SAW) acoustophoresis: now and beyond. Lab Chip 12:2766–2770

Liu C, Hu G, Jiang X, Sun J (2015a) Inertial focusing of spherical particles in rectangular microchannels over a wide range of Reynolds numbers. Lab Chip 15:1168–1177

Liu C, Xue C, Chen X, Shan L, Tian Y, Hu G (2015b) Size-based separation of particles and cells utilizing viscoelastic effects in straight microchannels. Anal Chem 87:6041–6048

Liu C, Xue C, Sun J, Hu G (2016) A generalized formula for inertial lift on a sphere in microchannels. Lab Chip 16:884–892

Lu X, Xuan X (2015) Inertia-enhanced pinched flow fractionation. Anal Chem 87:4560–4565

Lu X, Zhu L, Hua R, Xuan X (2015) Continuous sheath-free separation of particles by shape in viscoelastic fluids. Appl Phys Lett 107:264102

Martel JM, Toner M (2013) Particle focusing in curved microfluidic channels. Sci Rep 3:3340. doi:10.1038/srep03340

Martel JM, Toner M (2014) Inertial focusing in microfluidics. Annu Rev Biomed Eng 16:371–396

Nguyen NT (2012) Micro-magnetofluidics: interactions between magnetism and fluid flow on the microscale. Microfluid Nanofluid 12:1–16

Oakey J, Applegate RW Jr, Arellano E, Carlo DD, Graves SW, Toner M (2010) Particle focusing in staged inertial microfluidic devices for flow cytometry. Anal Chem 82:3862–3867

Ozkumur E, Shah AM, Ciciliano JC, Emmink BL, Miyamoto DT, Brachtel E, Yu M, Chen P, Morgan B, Trautwein J, Kimura A, Sengupta S, Stott SL, Murat Karabacak N, Barber TA, Walsh R, Smith K, Spuhler PS, Sullivan JP, Lee RJ, Ting DT, Luo X, Shaw AT, Bardia A, Sequist LV, Louis DN, Maheswaran S, Kapur R, Haber DA, Toner M (2013) Inertial focusing for tumor antigen–dependent and independent sorting of rare circulating tumor cells. Sci Translat Med 5:179ra47. doi:10.1126/scitranslmed.3005616

Pamme N (2006) Magnetism and microfluidics. Lab Chip 6:24–38

Pamme N (2007) Continuous flow separations in microfluidic devices. Lab Chip 7:1644–1659

Pamme N, Manz A (2004) On-chip free-flow magnetophoresis: continuous flow separation of magnetic particles and agglomerates. Anal Chem 76:7250–7256

Pethig R (2010) Review article—dielectrophoresis: status of the theory, technology, and applications. Biomicrofluid 4:022811

Romeo G, D'Avino G, Greco F, Nettiab PA, Maffettone PL (2013) Viscoelastic flow-focusing in microchannels: scaling properties of the particle radial distributions. Lab Chip 13:2802–2807

Rosensweig RE (1987) Magnetic fluids. Annu Rev Fluid Mech 19:437–461

Sajeesh P, Sen AK (2014) Particle separation and sorting in microfluidic devices: a review. Microfluid Nanofluid 17:1–52

Shen F, Hwang H, Hahn YK, Park JK (2012) Label-free cell separation using a tunable magnetophoretic repulsion force. Anal Chem 84:3075–3081

Shields CW IV, Reyes CD, López GP (2015) Microfluidic cell sorting: a review of the advances in the separation of cells from debulking to rare cell isolation. Lab Chip 15:1230–1249

Suwa M, Watarai H (2011) Magnetoanalysis of micro/nanoparticles: a review. Anal Chim Acta 690:137–147

Tarn MD, Hirota N, Iles A, Pamme N (2009) On-chip diamagnetic repulsion in continuous flow. Sci Technol Adv Mater 10:014611

Tsai C, Chen H, Wang Y, Lin C, Fu L (2007) Capabilities and limitations of 2-dimensional and 3-dimensional numerical methods in modeling the fluid flow in sudden expansion microchannels. Microfluid Nanofluid 3:13–18

Tsutsui H, Ho CM (2009) Cell separation by non-inertial force fields in microfluidic systems. Mech Res Commun 36:92–103

Vojtíšek M, Tarn MD, Hirota N, Pamme N (2012) Microfluidic devices in superconducting magnets: on-chip free-flow diamagnetophoresis of polymer particles and bubbles. Microfluid Nanofluid 13:625–635

Wang X, Zandi M, Ho CC, Kaval N, Papautsky I (2015) Single stream inertial focusing in a straight microchannel. Lab Chip 15:1812–1821

Watarai H (2013) Continuous separation principles using external microaction forces. Annu Rev Anal Chem 6:353–378

Xiang N, Dai Q, Ni Z (2016a) Multi-train elasto-inertial particle focusing in straight microfluidic channels. Appl Phys Lett 109:134101

Xiang N, Zhang X, Dai Q, Cheng J, Chen K, Ni Z (2016b) Fundamentals of elasto-inertial particle focusing in curved microfluidic channels. Lab Chip 16:2626–2635

Yamada M, Seki M (2005) Hydrodynamic filtration for on-chip particle concentration and classification utilizing microfluidics. Lab Chip 5:1233–1239

Yamada M, Nakashima M, Seki M (2004) Pinched flow fractionation: continuous size separation of particles utilizing a laminar flow profile in a pinched microchannel. Anal Chem 76:5465–5471

Yan S, Zhang J, Yuan D, Li W (2016) Hybrid microfluidics combined with active and passive approaches for continuous cell separation. Electrophoresis. doi:10.1002/elps.201600386

Yang SY, Kim JY, Lee SJ, Lee SS, Kim JM (2011) Sheathless elasto-inertial particle focusing and continuous separation in a straight rectangular microchannel. Lab Chip 11:266–273

Yang R, Hou H, Wang Y, Fu L (2016) Micro-magnetofluidics in microfluidic systems: a review. Sens Actuat B 224:1–15

Yuan D, Zhang J, Yan S, Pan C, Alici G, Nguyen NT, Li WH (2015) Dean-flow-coupled elasto-inertial three-dimensional particle focusing under viscoelastic flow in a straight channel with asymmetrical expansion–contraction cavity arrays. Biomicrofluid 9:044108

Zeng J, Deng Y, Vedantam P, Tzeng TR, Xuan X (2013) Magnetic separation of particles and cells in ferrofluid flow through a straight microchannel using two offset magnets. J Magn Magn Mater 346:118–123

Zhang J, Yan S, Yuan D, Alici G, Nguyen NT, Warkiani ME, Li W (2016a) Fundamentals and applications of inertial microfluidics: a review. Lab Chip 16:10–34

Zhang J, Yan S, Yuan D, Zhao Q, Tan SH, Nguyen NT, Li W (2016b) A novel viscoelastic-based ferrofluid for continuous sheathless microfluidic separation of nonmagnetic microparticles. Lab Chip 16:3947–3956

Zhao W, Cheng R, Miller J, Mao L (2016a) Label-free microfluidic manipulation of particles and cells in magnetic liquids. Adv Funct Mater 26:3916–3932

Zhao W, Zhu T, Cheng R, Liu Y, He J, Qiu H, Wang L, Nagy T, Querec TD, Unger ER, Mao L (2016b) Label-free and continuous-flow ferrohydrodynamic separation of HeLa cells and blood cells in biocompatible ferrofluids. Adv Funct Mater 26:3990–3998

Zhou J, Papautsky I (2013) Fundamentals of inertial focusing in microchannels. Lab Chip 13:1121–1132

Zhou R, Wang C (2016a) Microfluidic separation of magnetic particles with soft magnetic microstructures. Microfluid Nanofluid 20:1–11

Zhou R, Wang C (2016b) Multiphase ferrofluid flows for micro-particle focusing and separation. Biomicrofluid 10:034101

Zhou Y, Xuan X (2016) Diamagnetic particle separation by shape in ferrofluids. Appl Phys Lett 109:102405

Zhou J, Giridhar PV, Kasper S, Papautsky I (2013) Modulation of aspect ratio for complete separation in an inertial microfluidic channel. Lab Chip 13:1919–1929

Zhou Y, Kumar DT, Lu X, Kale A, DuBose J, Song Y, Wang J, Li D, Xuan X (2015) Simultaneous diamagnetic and magnetic particle trapping in ferrofluid microflows via a single permanent magnet. Biomicrofluid 9:044102

Zhou Y, Song L, Yu L, Xuan X (2016) Continuous-flow sheathless diamagnetic particle separation in ferrofluids. J Magn Magn Mater 412:114–122

Zhu T, Marrero F, Mao L (2010) Continuous separation of non-magnetic particles inside ferrofluids. Microfluid Nanofluid 9:1003–1009

Zhu J, Liang L, Xuan X (2012a) On-chip manipulation of nonmagnetic particles in paramagnetic solutions using embedded permanent magnets. Microfluid Nanofluid 12:65–73

Zhu T, Cheng R, Lee SA, Rajaraman E, Eiteman MA, Querec TD, Unger ER, Mao L (2012b) Continuous-flow ferrohydrodynamic sorting of particles and cells in microfluidic devices. Microfluid Nanofluid 13:645–654

Zhu T, Cheng R, Liu Y, He J, Mao L (2014) Combining positive and negative magnetophoreses to separate particles of different magnetic properties. Microfluid Nanofluid 17:973–982